Electronic Supplementary Information

Synthesis of shape-tunable $PbZrTiO_3$ nanocrystals with lattice variations for piezoelectric energy harvesting and human motion detection

Ya-Ju Chuang, Arnab Pal, Bo-Hao Chen, Satyaranjan Jena, Sreerag Suresh, Zong-Hong Lin and Michael H. Huang**

Chemicals

Lead nitrate ($Pb(NO_3)_2$, J. T. Baker), zirconyl chloride octahydrate ($ZrOCl_2 \cdot 8H_2O$, 98%, Sigma-Aldrich), titanium bis(ammonium lactato)dihydroxide solution ($[CH_3CH(O-)CO_2NH_4]_2Ti(OH)_2$, TALH, 50 wt. %, Sigma-Aldrich), potassium hydroxide (KOH, ≥85%, Honeywell), acetic acid (CH_3COOH, ≥99.8%, Honeywell), lithium nitrate, anhydrous ($LiNO_3$, 99%, Alfa Aesar), polydimethylsiloxane (PDMS, DOWSIL^{TW} 184 silicon elastomer base and silicone elastomer curing agent, DOW Corning Corporation), and FE-3612-OE-B ITO film (Acute Touch Technology Co.).

Piezoelectric force microscopy measurements

The system was operated in contact mode using Pt/Ir-coated silicon-based conductive AFM tips (OSCM-PIT) with a force constant of 3 N/m, and at an AC voltage of 1 V and operating frequency of 77 kHz. Prior to measurements, $PbZrTiO_3$ crystals were thoroughly dispersed and attached to a Si substrate by spin coating. To maintain consistent environmental conditions, we utilized a dehumidifier system and monitored the condition using a digital hygrometer/thermometer. All measurements were conducted at room temperature (25 ± 0.5 ºC) and 41 ± 5% relative humidity, as verified by the digital display shown in Fig. S10. Scanning was performed at a rate of 0.5 Hz with an applied force of 100 nN over a 1 μm × 1 μm scan area. Both trace and retrace signals were recorded to ensure measurement reliability. The complete experimental setup (Fig. S10) shows the AFM system, environmental control equipment, and monitoring devices to aid readers in understanding the measurement configuration.

Electrical measurements and real-time movement detection

For human movement detection, the output voltage of the developed PENG was measured by the shoe insole integrated system. This system is comprised of a parallel RC circuit, an AD620 amplifier, and a NI myRIO module from National Instruments. Its purpose is to convert the analog signals produced by the sensor into digital signals, ensuring a reliable and synchronous data acquisition process. The data was transmitted wirelessly between the PENG and the laptop *via* the NI myRIO's wireless module. A programmed system based on the LabVIEW platform and a machine

learning model was employed to analyze the data acquired by the PENG device.

Practical validation of PENG output energy utilization

The digital hygrometer we used requires an operating voltage of 1.5 V DC and has a power consumption of approximately 50-100 μW during active measurement. The digital stopwatch operates at 1.2V DC with a power consumption of around 30–50 μW in normal operation. Using a 1.0 μF capacitor charged by the PENG, which generated a peak voltage of 20.36 V and current of 230 nA, we were able to:

1. Power the hygrometer for approximately 1–2 seconds per full charge.
2. Operate the stopwatch for about 2–3 seconds per charge.

Stable device operation through the rectified and regulated output was achieved. The relatively low power consumption of these commercial electronic devices matches with our PENG's output capabilities (2.4 μW maximum power at 986 KΩ load resistance). This alignment enables practical demonstration while still being within the typical range for self-powered wearable devices.[1] For continuous long-term operation, multiple capacitors could be used in parallel to provide a more stable power supply, similar to approaches used in other piezoelectric energy harvesting systems.[2]

References

1 Y. Bai, H. Jantunen and J. Juuti, *Adv. Mater.*, 2018, **30**, 1707271.

2 C. Wu, P. Jiang, W. Li, H. Guo, J. Wang, J. Chen, M. R. Prausnitz and Z. L. Wang, *Adv. Funct. Mater.*, 2020, **30**, 1907378.

Table S1 Complete synthetic conditions for the growth of $PbZrTiO_3$ crystals with tunable sizes, shapes, and compositions.

Size	H_2O	TALH	0.65 M $ZrOCl_2$	$Pb(NO_3)_2$	KOH	$LiNO_3$	T (°C)	T (h)
538 nm cubes					0.5 M 10 mL	w/o		
413 nm cubes	1 mL	100.3 µL	500 µL	0.2898 g	0.5 M 10 mL	0.45 M 500 µL	200	2.5
282 nm cubes					0.35 M 15 mL	1.0 M 2000 µL		

Shape	H_2O	TALH	0.65 M $ZrOCl_2$	$Pb(NO_3)_2$	0.5 M KOH	T (°C)	T (h)
cubes	1 mL	66.9 µL	400 µL	0.2898 g	10 mL	200	2.5
cuboids		117 µL	700 µL				

Zr:Ti	H_2O	TALH	0.65 M $ZrOCl_2$	$Pb(NO_3)_2$	0.35 M KOH	0.45 M $LiNO_3$	T (°C)	T (h)
60:40	1 mL	150 µL	450 µL		15 mL			
55:45	1 mL	170 µL	430 µL	0.2898 g	15 mL	500 µL	200	2.5
45:55	1 mL	200 µL	400 µL		10 mL			

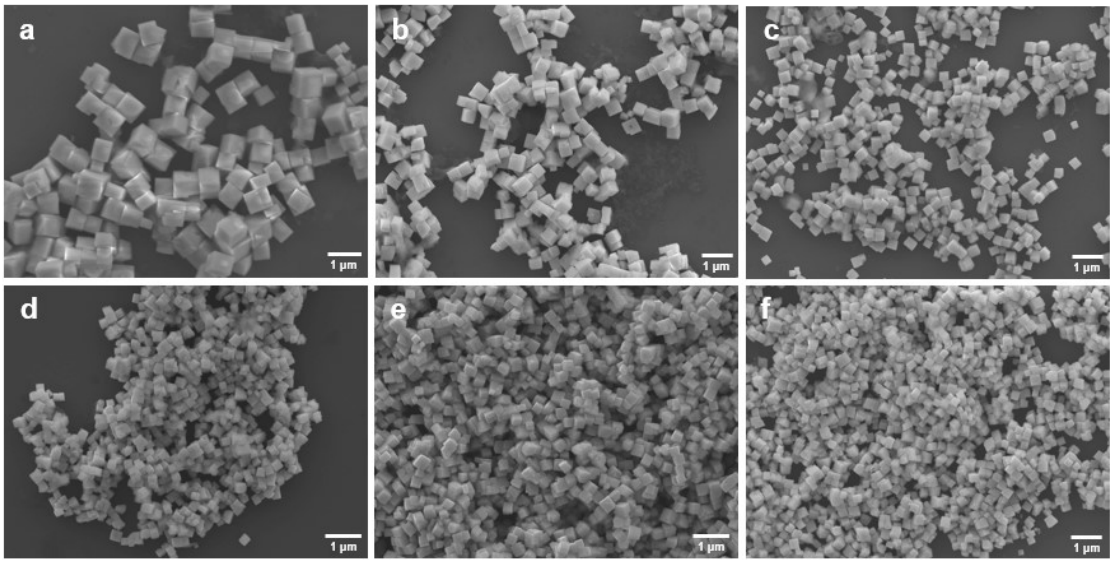

Fig. S1 (a–c) SEM images of $PbZr_{0.7}Ti_{0.3}O_3$ cubes with sizes of (a) 538, (b) 413, and (c) 282 nm. (d–f) SEM images of $PbZr_xTi_{1-x}O_3$ cubes with Zr:Ti atomic ratios of (d) 60:40, (e) 55:45, and (f) 45:55.

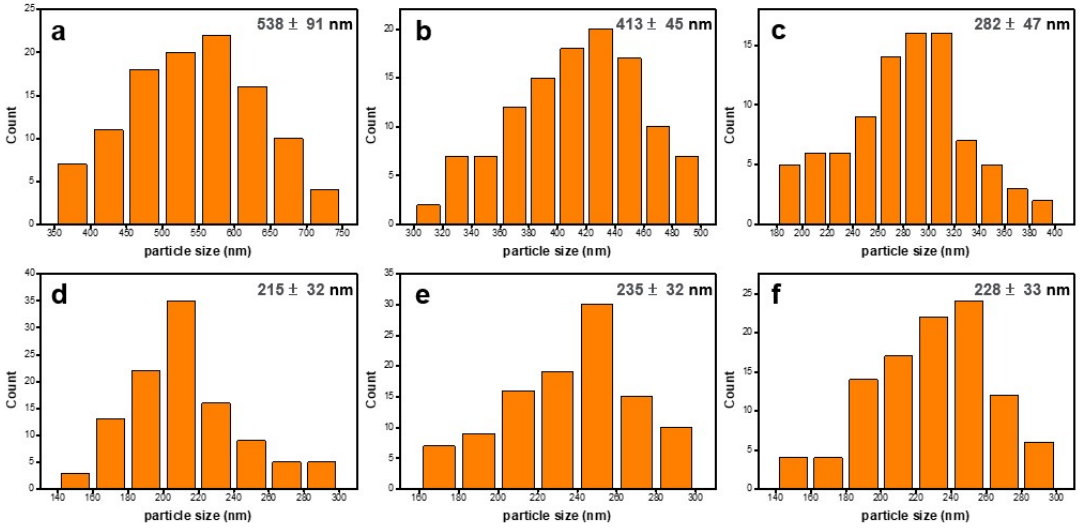

Fig. S2 Size distribution histograms of (a) 538, (b) 413, and (c) 282 nm $PbZr_{0.7}Ti_{0.3}O_3$ cubes, (d) $PbZr_{0.6}Ti_{0.4}O_3$ cubes, (e) $PbZr_{0.55}Ti_{0.45}O_3$ cubes, and (f) $PbZr_{0.45}Ti_{0.55}O_3$ cubes.

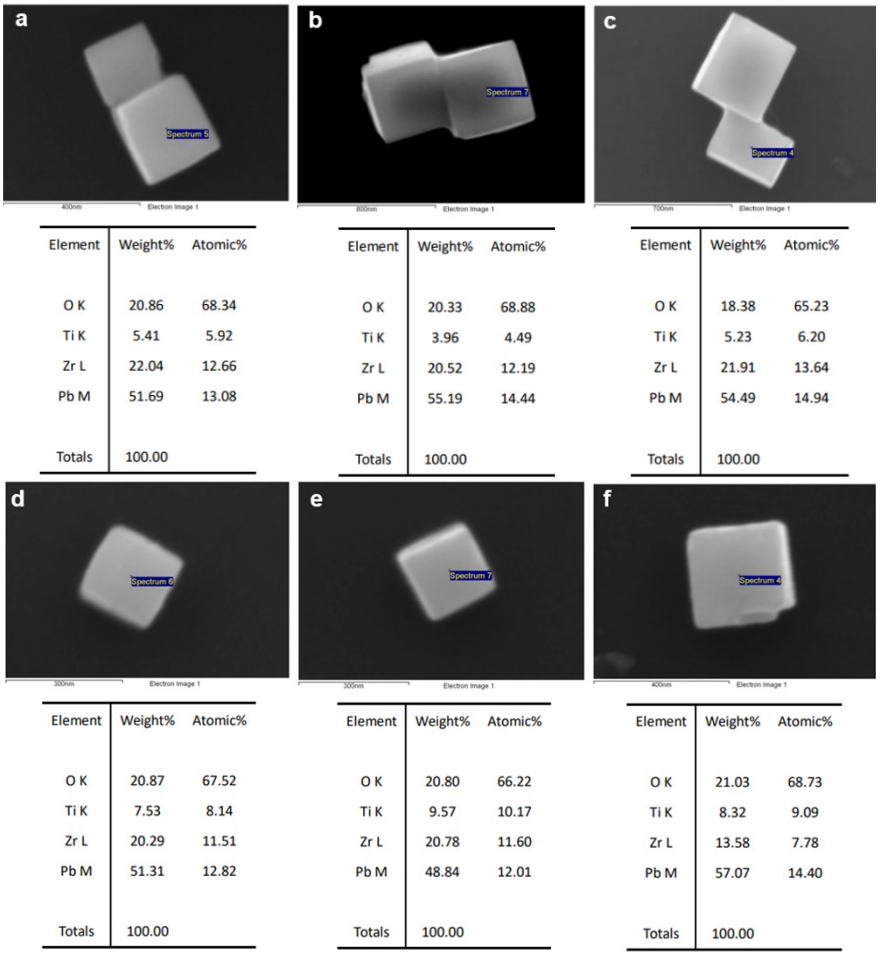

Element	Weight%	Atomic%
O K	20.86	68.34
Ti K	5.41	5.92
Zr L	22.04	12.66
Pb M	51.69	13.08
Totals	100.00	

Element	Weight%	Atomic%
O K	20.33	68.88
Ti K	3.96	4.49
Zr L	20.52	12.19
Pb M	55.19	14.44
Totals	100.00	

Element	Weight%	Atomic%
O K	18.38	65.23
Ti K	5.23	6.20
Zr L	21.91	13.64
Pb M	54.49	14.94
Totals	100.00	

Element	Weight%	Atomic%
O K	20.87	67.52
Ti K	7.53	8.14
Zr L	20.29	11.51
Pb M	51.31	12.82
Totals	100.00	

Element	Weight%	Atomic%
O K	20.80	66.22
Ti K	9.57	10.17
Zr L	20.78	11.60
Pb M	48.84	12.01
Totals	100.00	

Element	Weight%	Atomic%
O K	21.03	68.73
Ti K	8.32	9.09
Zr L	13.58	7.78
Pb M	57.07	14.40
Totals	100.00	

Fig. S3 SEM images and EDS analysis results of (a) a 282 nm $PbZr_{0.7}Ti_{0.3}O_3$ cube, (b) a 555 nm $PbZr_{0.7}Ti_{0.3}O_3$ cube, (c) a 660 nm $PbZr_{0.7}Ti_{0.3}O_3$ cuboid, (d) a $PbZr_{0.6}Ti_{0.4}O_3$ cube, (e) a $PbZr_{0.55}Ti_{0.45}O_3$ cube, and (f) a $PbZr_{0.45}Ti_{0.55}O_3$ cube.

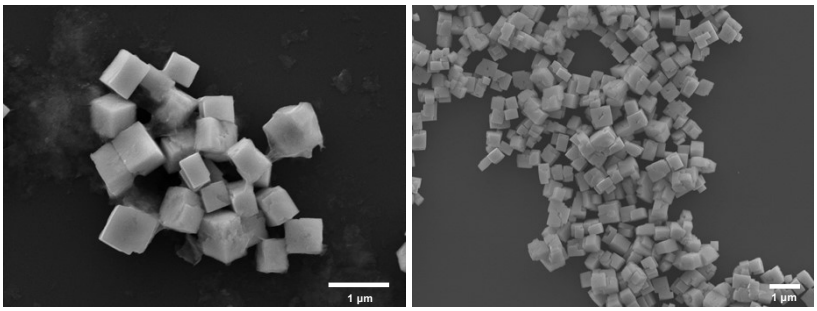

Fig. S4 Additional SEM images of the $PbZr_{0.7}Ti_{0.3}O_3$ cuboids.

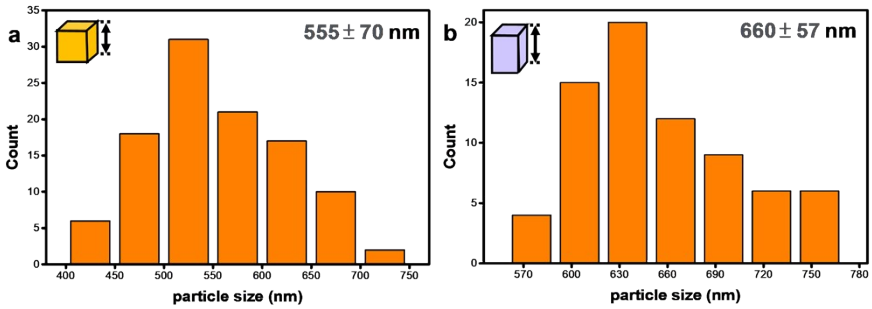

Fig. S5 Size distribution histograms of $PbZr_{0.7}Ti_{0.3}O_3$ (a) cubes and (b) cuboids.

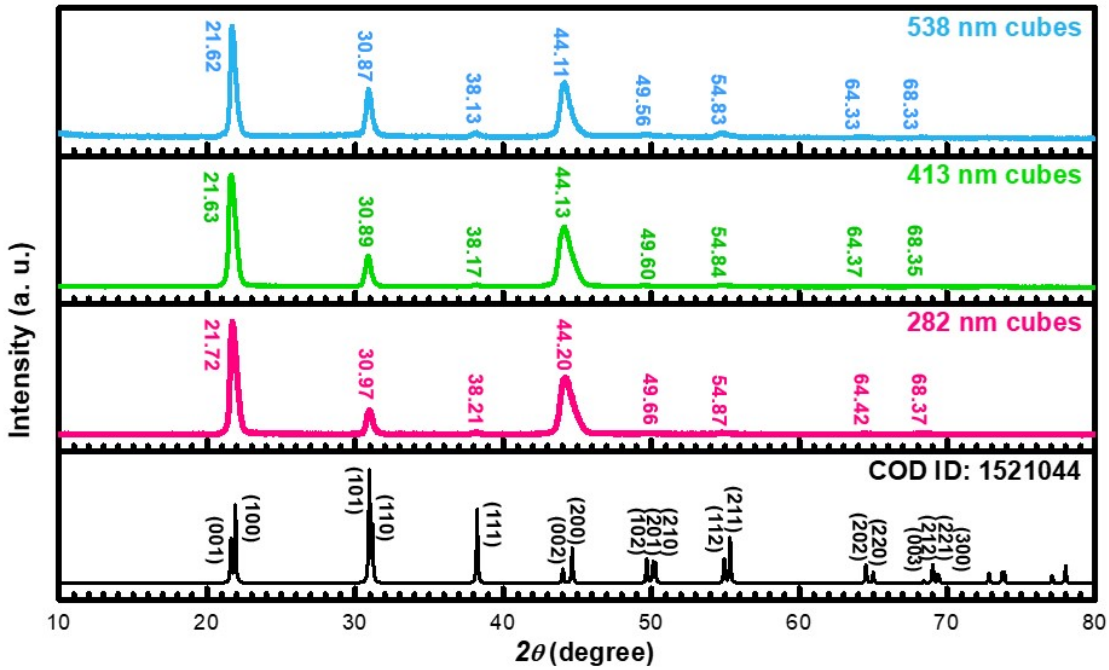

Fig. S6 XRD patterns of the size-tunable $PbZr_{0.7}Ti_{0.3}O_3$ cubes. A tetragonal phase reference pattern of $PbZrTiO_3$ is also provided.

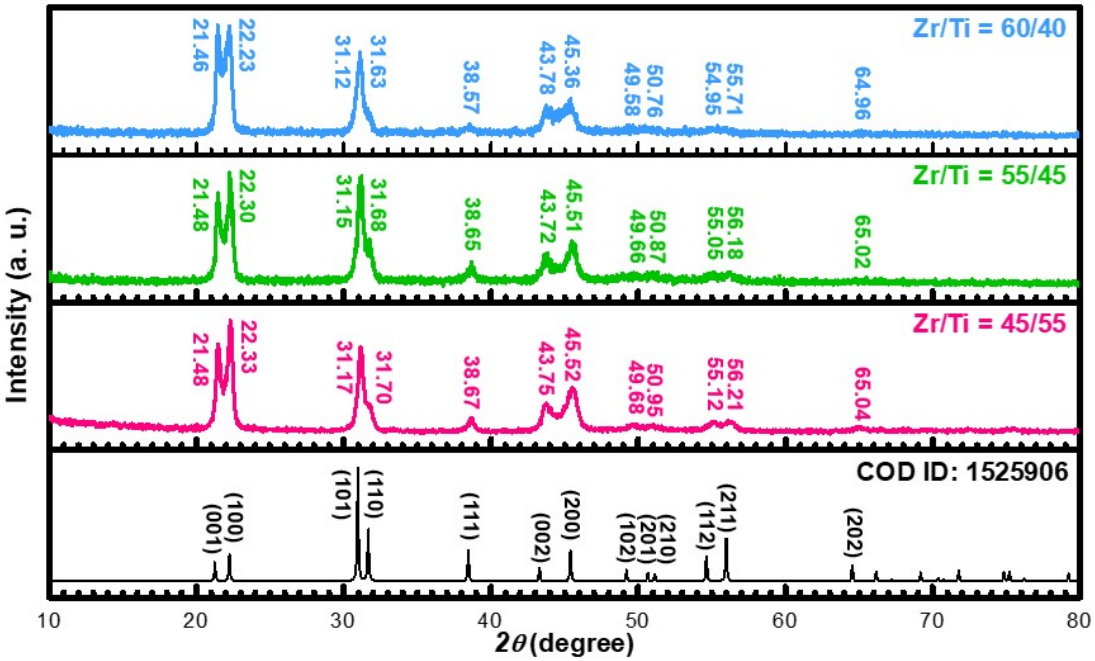

Fig. S7 XRD patterns of the $PbZ_{0.6}Ti_{0.4}O_3$, $PbZ_{0.55}Ti_{0.45}O_3$, and $PbZ_{0.45}Ti_{0.55}O_3$ cubes and the tetragonal phase reference.

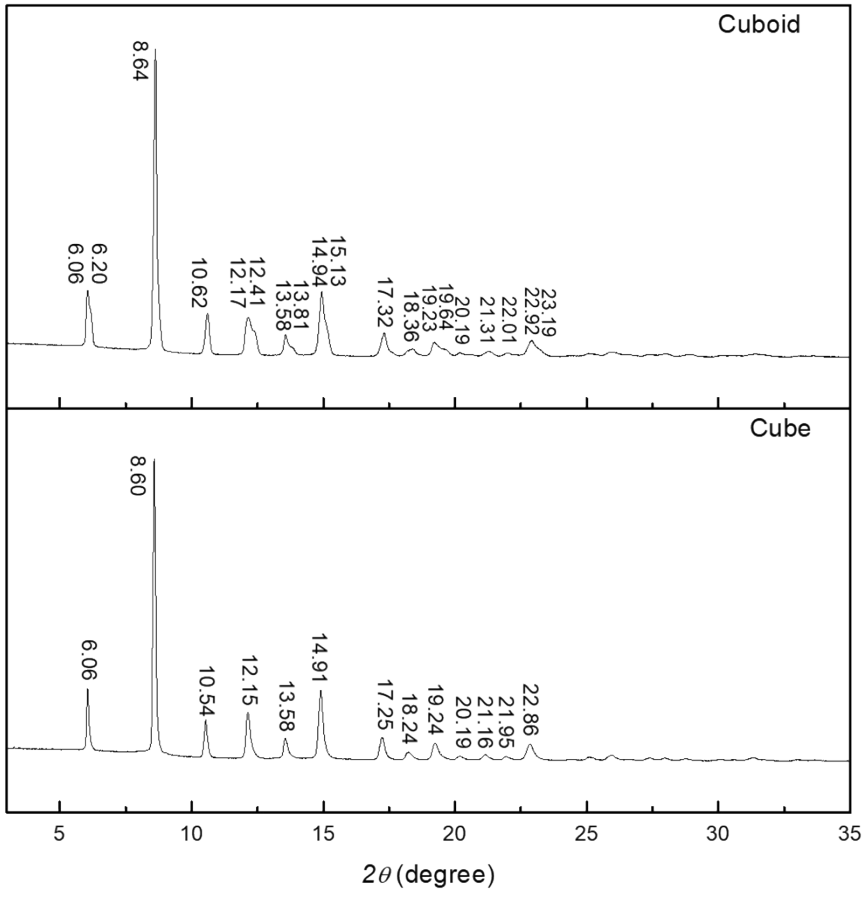

Fig. S8 Full synchrotron XRD patterns of $PbZr_{0.7}Ti_{0.3}O_3$ cuboids and cubes.

Table S2 Lattice parameters and the refinement results of different $PbZrTiO_3$ samples.

Sample formula	$PbZr_{0.7}Ti_{0.3}O_3$				$PbZr_{0.6}Ti_{0.4}O_3$		$PbZr_{0.55}Ti_{0.45}O_3$		$PbZr_{0.45}Ti_{0.55}O_3$	
Morphology	Cubes		Cuboids		Cubes					
λ (Å)	0.43503									
Crystal system	Tetragonal									
Space group	P 4 m m									
Z (cell formula units)	1									
Temperature (K)	300 (roomtemperature)									
2θ (deg)	5-34.5									
Phase	Surface	Bulk	Surface	Bulk	Surface	Bulk	Surface	Bulk	Surface	Bulk
Phase fraction	0.600(6)	0.400(6)	0.705(4)	0.295(4)	0.110(4)	0.890(4)	0.282(6)	0.718(6)	0.259(6)	0.741(6)
a, *b* (Å)	4.08467(29)	4.11164(21)	4.0417(3)	4.09143(17)	3.9805(3)	4.0109(3)	3.97329(24)	4.0023(3)	3.97238(22)	3.99902(31)
c (Å)	4.12603(23)	4.14270(23)	4.13580(25)	4.13533(30)	4.1299(7)	4.13364(26)	4.1341(5)	4.13461(26)	4.1338(5)	4.13484(22)
c/*a*	1.01013	1.00755	1.02328	1.01073	1.03764	1.02896	1.04047	1.03306	1.04064	1.03396
α (°)	90									
β (°)	90									
γ (°)	90									
Volume (Å^3)	68.841(11)	70.035(10)	67.559(12)	69.225(7)	65.436(14)	66.500(13)	65.265(10)	66.229(12)	65.230(10)	66.125(11)
d-spacing resolution (Å)	0.746		0.738		0.735		0.734		0.738	
Unique axis [hkl]	[001]									
Equatorial μ strain (Δ*d*/*d*)	0.0263	0.0139	0.0422	0.0174	0.0072	0.0415	0.0108	0.0336	0.0103	0.0351
Axial μ strain (Δ*d*/*d*)	0.0112	0.0097	0.0168	0.0197	0.0701	0.0165	0.0425	0.0166	0.0565	0.0161
Zero point shift (°)	0.0156		-0.0057		-0.0064		-0.0043		-0.0040	
wR (%)	5.430		5.234		6.982		7.464		6.893	
R (F^2) (%)	3.599	3.618	3.663	3.559	6.818	4.968	6.594	5.109	6.293	5.016

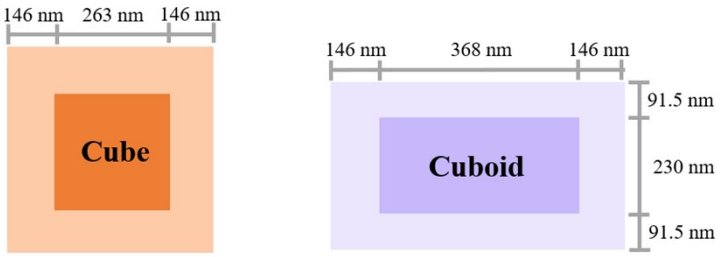

Fig. S9 Dimensions of bulk and surface phases of $PbZr_{0.7}Ti_{0.3}O_3$ cuboids and cubes constructed using the synchrotron XRD data with phase fractions.

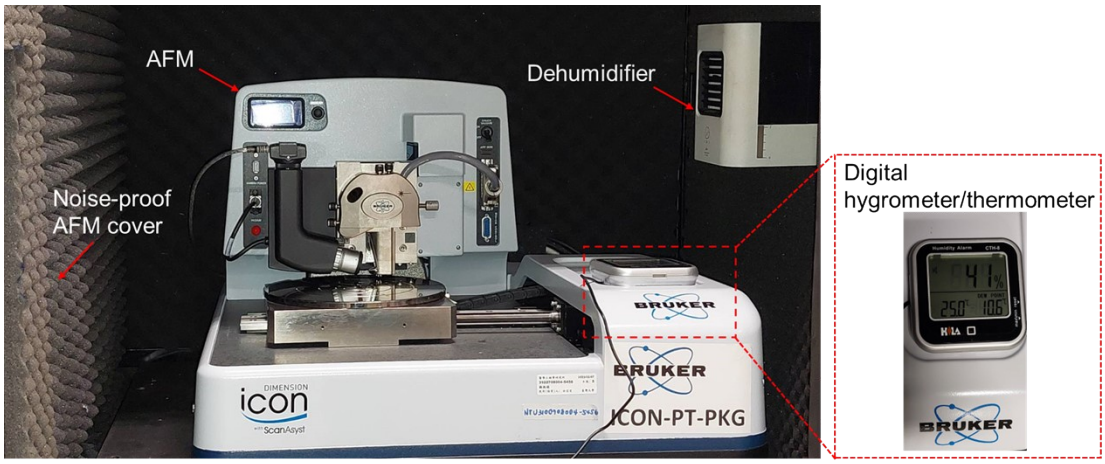

Fig. S10 Experimental setup for PFM measurements showing the Bruker Dimension Icon AFM system with its key components.

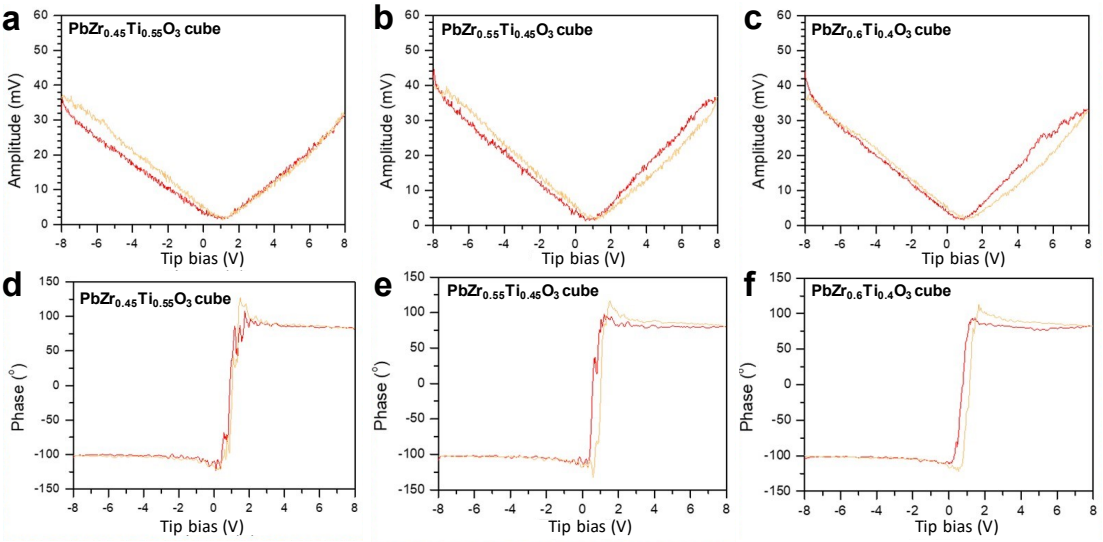

Fig. S11 (a–c) Piezoelectric butterfly loops of $PbZr_{0.45}Ti_{0.55}O_3$, $PbZr_{0.55}Ti_{0.45}O_3$, and $PbZr_{0.6}Ti_{0.4}O_3$ cubes. (d–f) Ferroelectric hysteresis loops of these crystals.

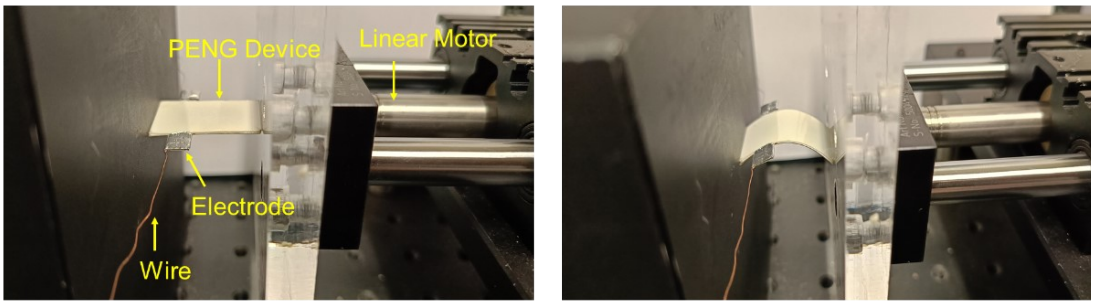

Fig. S12 Photographs of the PENG device for measurements of mechanical-to-electrical energy conversion.

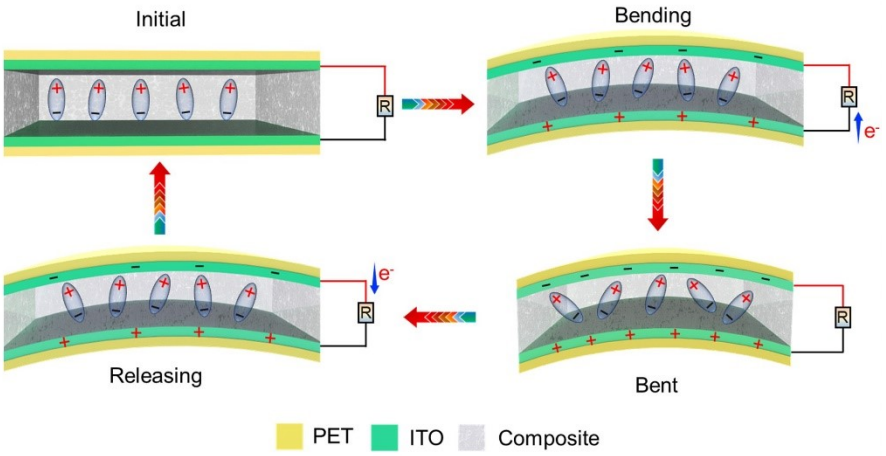

Fig. S13 Schematic illustration of cyclic bend-release process of the PENG device.

Table S3 Output voltages and currents of PENG devices fabricated using $PbZr_{0.7}Ti_{0.3}O_3$ cubes and cuboids with different weight percentages.

$PbZrTiO_3$ weight percentage	Cubes		Cuboids	
	Voltage (V)	Current (nA)	Voltage (V)	Current (nA)
10 wt.%	11.58	320	13.05	920
20 wt.%	11.93	1180	15.89	1300
30 wt.%	14.13	1610	20.36	2300
40 wt.%	12.46	1350	19.13	1620

Table S4 Comparison of the output performance of PENGs fabricated with different $PbZrTiO_3$ morphologies.

	Porous PZT-PDMS	PZT-PDMS	PZT-Film	PZT-PDMS	
Morphology	irregular particles	nanowires	film	cubes	cuboids
Output Voltage	29 V	1 V	2 V	14.13 V	20.36 V
Output Current	0.116 μA	0.045 μA	0.25 μA	1.61 μA	2.3 μA
Reference	19	20	21	This work	This work

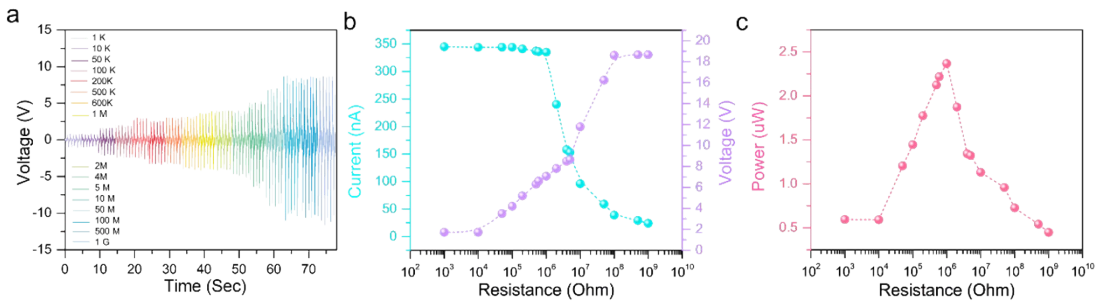

Fig. S14 (a) Output voltages for different external load resistances. (b) Variation in output voltage and current under different load resistances. (c) Mathematically calculated effective power output curve with respect to load resistance.

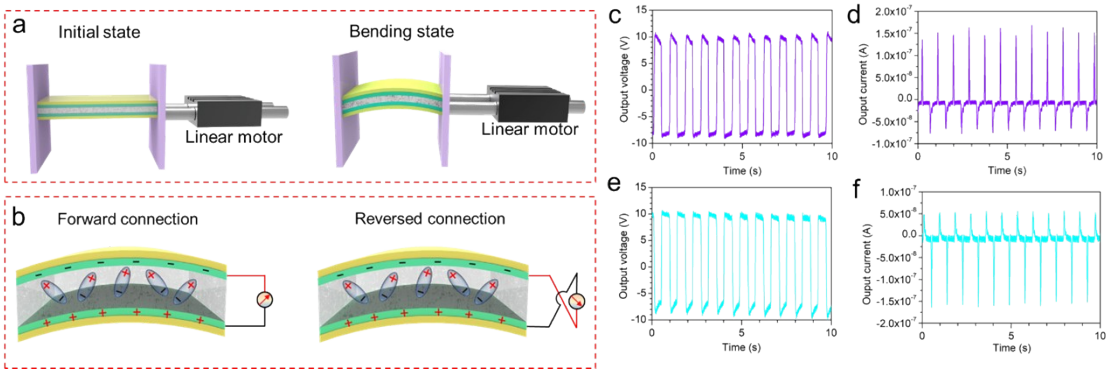

Fig. S15 (a) Diagram of bending motion of the PENG, executed by a linear motor. (b) Circuit connection diagram for the forward and reverse connection polarity switching experiment. (c, d) The forward voltage and current. (e, f) The reverse voltage and current.

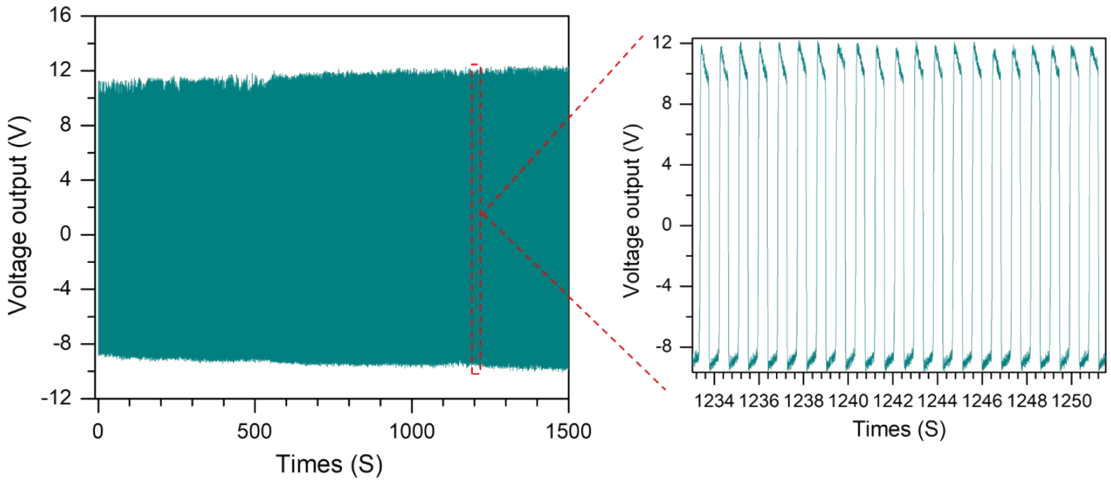

Fig. S16 Stability test of the fabricated PENG device with 30 wt. % $PbZrTiO_3$ cuboids over 1500 sec.

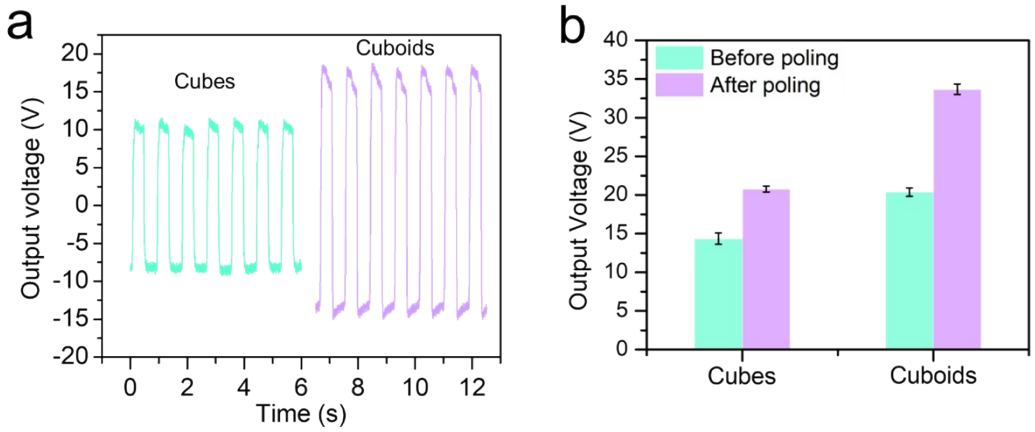

Fig. S17 (a) Open-circuit voltages after poling. (b) Comparison of open-circuit voltages before and after poling.

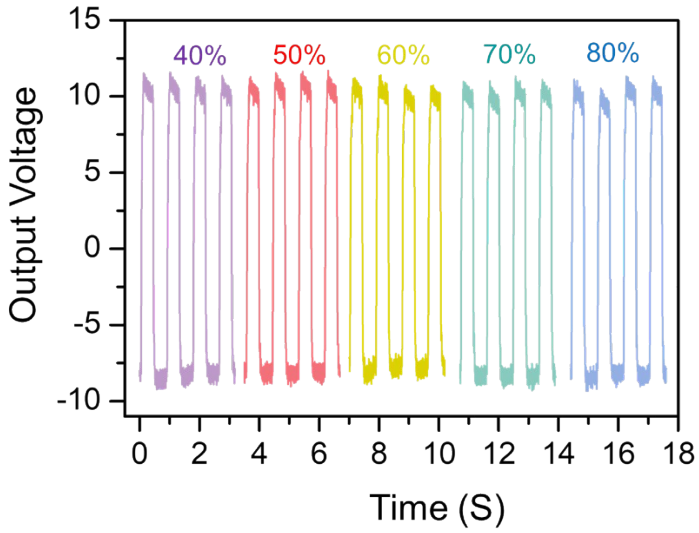

Fig. S18 Humidity-dependent output voltages showing stable output of the device.

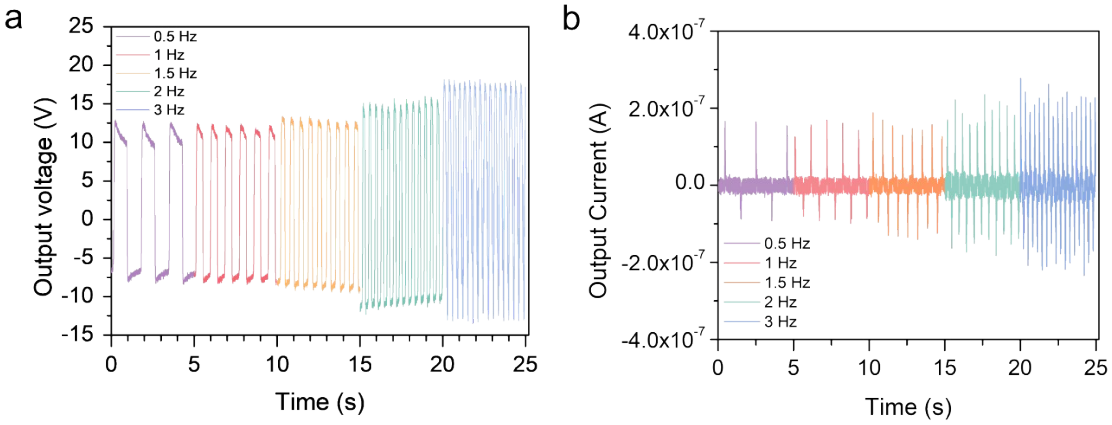

Fig. S19 Frequency-dependent (a) output voltage and (b) output current of the device.

Table S5. Comparison of the output performance of PENGs fabricated with other state-of-the-art PENGs using different materials.

Material system	Morphology	Open-circuit voltage (V)	Current density/Current output	Architecture	Reference
$PbZrTiO_3$	cuboids	20.36	38.3 nA/cm²	PDMS composite	present work
PMN-PT	nanowires	7.8	2.29 μA	PDMS composite	29
$ZnSnO_3$	nanocubes	20.0	0.9 μA/cm²	PDMS composite	30
$LiNbO_3$	nanowires	0.46	9.11 nA	PDMS composite	31
$NaNbO_3$	nanowires	3.2	16 nA/cm²	PDMS composite	32
$FAPbBr_3$	nanoparticles	8.5	3.4 μA/cm²	PDMS composite	33

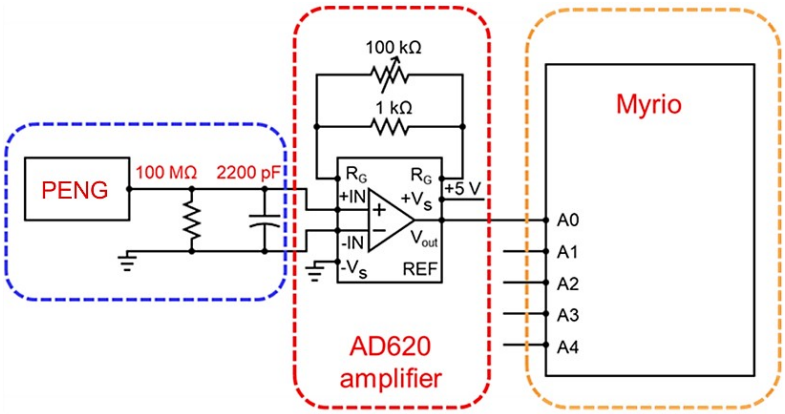

Fig. S20 Representative electrical circuit diagram of the wireless signal transmission system.

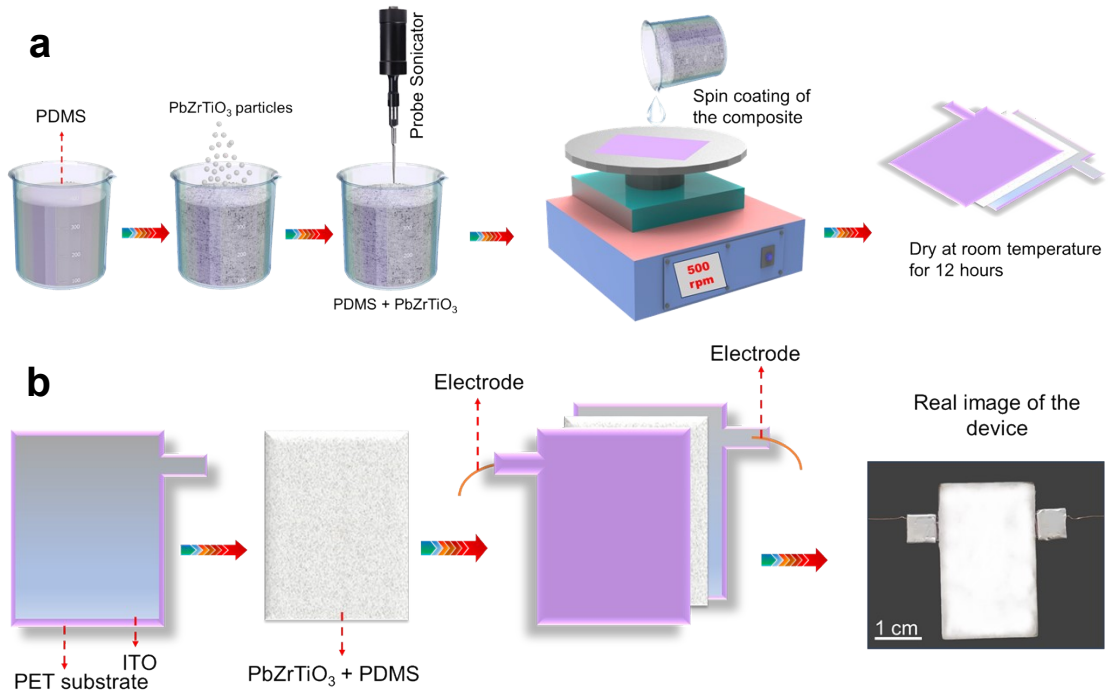

Fig. S21 (a) Schematic illustration of the fabrication process of a piezoelectric nanogenerator. (b) Structure of the sandwich-like device and its photograph.